Pergamon

Int. J. Heat Mass Transfer. Vol. 40, No. 6, pp. 1365–1378, 1997

0017–9310/97 $17.00 + 0.00

PII: S0017-9310(96)00186-X

An experimental study of flow and heat transfer in parallel-plate arrays: local, row-by-row and surface average behavior

N. C. DEJONG and A. M. JACOBI†

Department of Mechanical and Industrial Engineering, 1206 West Green Street, The University of Illinois at Urbana-Champaign, Urbana, IL 61801, U.S.A.

(*Received* 1 *April* 1996 *and in final form* 23 *May* 1996)

Abstract—Detailed observations of flow through large arrays of flat plates are used with mass transfer experiments to explore the convective behavior in offset-strip geometries. Unique local data for individual plates in the array are obtained using the naphthalene sublimation technique. With the flow visualization results, these local data reveal the effects of boundary-layer growth and vortex shedding in the array. Row-by-row data are used to determine the onset of shedding within the array. Surface average results are presented and show the relative contributions to heat transfer of boundary-layer restarting and vortex shedding. Copyright © 1996 Elsevier Science Ltd.

INTRODUCTION

In many compact heat exchanger applications, interrupted-fin surfaces are used to enhance the air-side heat transfer performance. Interrupted surfaces restart the boundary layers and, since the average boundary layer thickness is smaller for short plates than for long plates, the average heat transfer coefficient is higher for an interrupted surface than for a continuous surface. Furthermore, above some critical Reynolds number, interrupted surfaces can cause vortex shedding. The self-sustained flow oscillations associated with vortex shedding enhance heat transfer. Interrupted surfaces usually take the form of offset-strip or louvered-fin designs; offset-strip fins are aligned with the main flow, but louvered fins usually have an angle of attack. This research focuses on the offset-strip geometry. There has been extensive prior research on interrupted surfaces in an offset-strip arrangement. A thorough review of the literature was recently provided by Manglik and Bergles [1]; therefore, only a survey to place the current work in context will be provided.

Sparrow and Hajiloo [2] analyzed staggered-plate geometries for Reynolds numbers from 1000 to 9000 based on hydraulic diameter. They used the naphthalene sublimation method but utilized only one test plate per array. They found the thermally developing region to be only one row deep in the 'periodic fully developed regime', which they defined as fully developed with streamwise velocity variations due to periodic changes in geometry. They found plate thickness to have little effect on the Nusselt number for $Re < 1200$, but at higher Reynolds numbers, the Nusselt number increased faster with Reynolds number for thicker plates. For the thickest plates, the friction factor, f, was independent of the Reynolds number. For thin plates, however, f decreased smoothly with an increase in Reynolds number.

Mochizuki and co-workers [3, 4] visualized flow through offset-strip fins for a variety of conditions ranging from a single plate to twenty rows of plates. They used dye and hydrogen bubbles to visualize the flow in a water tunnel and a hot-wire anemometer to measure the vortex shedding frequency in a wind tunnel. For a single plate, at $Re_t = 250$, the Strouhal number dropped from approximately 0.18 to 0.16 and then remained constant for further increases in Re_t. They suggested that the separation point moved from the trailing to the leading edge of the plate at this Re_t. Mochizuki and Yagi stated that for two rows, two Strouhal numbers were present because each row generated a wake. With three to eight rows, one Strouhal number was present at low Reynolds numbers, but multiple Strouhal numbers occurred at higher Reynolds numbers. For nine to twenty rows, they found the Strouhal number to be constant at 0.13. They observed that as the Reynolds number increased, the onset of vortex shedding moved upstream in the array. Three regimes were present in the flow: steady laminar, oscillating and turbulent. When the Reynolds number was small, a small increase in the Reynolds number caused vortex shedding to begin much farther upstream, but when the Reynolds number was large, only minor changes in the flow field occurred when the Reynolds number was increased.

Mullisen and Loehrke [5] studied both in-line and staggered interrupted-plate arrays for a range of $100 < Re < 10\,000$. They used the Schlieren technique

† Author to whom correspondence should be addressed.

NOMENCLATURE

A	area
D_{na}	mass diffusion coefficient of naphthalene in air
d_h	hydraulic diameter, equation (2)
f	friction factor, equation (6)
h	local heat or mass transfer coefficient
$\bar{h}$	average heat or mass transfer coefficient
j	modified Colburn j factor, equation (5)
L	plate length, Fig. 2
L_{core}	length of heat exchanger core
m	mass
N	number of local data acquired during a surface scan
P	pressure
p_1, p_2	array dimensions relating to fin pitch, Fig. 2
Re	Reynolds number, based on hydraulic diameter unless otherwise noted, equation (1)
Sc	Schmidt number, v/D_{na}
Sh	local Sherwood number based on hydraulic diameter, equation (8)
$\overline{Sh}$	average Sherwood number based on hydraulic diameter, equation (4)
t	time or plate thickness, Fig. 2
U	average velocity
u	local streamwise (x-direction) velocity
x^*	dimensionless distance from the leading edge of a plate, x/L.

Greek symbols

δ_{sb}	local sublimation
v	kinematic viscosity
ρ	mass density.

Subscripts

c	evaluated at the minimum free-flow area of the heat exchanger
f	mass transfer surface
m	mass transfer
n, s	naphthalene in the solid phase
n, v	naphthalene in the vapor phase
t	fin thickness.

to visualize the flow and a transient heating technique to analyze heat transfer. In the in-line arrangement, they observed three regimes which they named steady, general unsteady and periodic unsteady. In the general unsteady regime, the wake had a wavy structure. The wake oscillations grew larger downstream, and sometimes flow across the entire passage appeared to be turbulent. The periodic unsteady regime was characterized by vortex shedding from the trailing edge of the plates. In contrast to earlier work [3], Mullisen and Loehrke concluded that for their shallow-array geometry the flow regime did not depend on streamwise location. They observed an increase in j and f at the transition to unsteady flow and theorized that this augmentation was due to increased mixing.

Joshi and Webb [6] modeled offset-strip fins using a combination of analytical and experimental techniques. Their model accounted for the finite thickness of the fins. They visualized the flow for three scaled-up geometries by injecting ink into water, and they divided the flow into four different regimes. In the first regime, the wake behind the upstream plate was smooth and laminar. In the second regime, oscillations were visible only where the flow impinged on the downstream plate. In the third, oscillations were present in the entire region between upstream and downstream plates, and in the fourth, vortices were shed. Their correlations for j and f in the laminar flow regime underpredicted the data at the onset of the second flow regime. Therefore, Joshi and Webb designated the Reynolds number at this point as the critical Reynolds number for transition from laminar to turbulent flow. From their analytical and experimental work, Joshi and Webb developed correlations to predict the transition from laminar to turbulent flow and to predict f and j for these two regimes.

Amon and Mikic [7] numerically modeled fully developed flow through a related communicating channel geometry. The geometry consisted of two infinite parallel plates a fixed distance apart, with a single column of aligned plates along the center of the channel. They found that above a critical Reynolds number, self-sustained laminar oscillations occurred in the flow at a frequency near the least stable Tollmien–Schlichting frequency. As a result of these oscillations and restarting of the boundary layer at each successive plate, heat transfer in this interrupted plate geometry was as much as 300% higher than in a flat plate geometry with the same pumping power. At low Reynolds numbers, they found two symmetrical standing eddies behind the plates. For slightly higher velocities, these eddies became unstable and began to change location and strength within the gap between plates. At higher Reynolds numbers yet, Amon and Mikic found that vortices were ejected alternately above and below the plates. These ordered oscillations resulted in a lower pumping power requirement than for turbulent flow. Amon *et al.* [8] visualized the flow in a communicating-channel geometry using real-time holographic interferometry. They concluded that the self-sustained oscillations and ejection of vortices increased heat transfer by increasing mixing and

affecting the flow impinging on the plate. They indicated that vortices delayed the formation of the thermal boundary layer, thus decreasing its overall thickness.

Xi *et al.* [9] visualized the flow in an offset-strip fin arrangement for $Re_t \leqslant 300$ by injecting ink into a water tunnel. They used a probe consisting of a hot- and cold-wire anemometer to measure velocity and temperature fluctuations. Like Joshi and Webb [6], they found that as the Reynolds number increased the flow went from a steady laminar flow to a flow in which the wakes exhibited either roughly sinusoidal fluid motion or the formation of discrete vortices. Referring to some of their earlier work, they suggested that heat transfer effects related to the formation of discrete vortices in the fin wakes caused j to deviate from the flat plate solution. As the fin pitch decreased, the flow transitions occurred at lower Reynolds numbers.

There have been very few studies of row-by-row heat transfer behavior in the offset-strip geometry†. Limited row-by-row data were presented by Kurosaki *et al.* [11] for a staggered arrangement of offset plates aligned with the flow. They attached heaters and thermocouples to some of the plates in their array. Row-by-row data were presented for a single geometry at only one Reynolds number (approximately 200) for five rows. They found that the heat transfer coefficient decreased slightly through the array. To the authors' knowledge, there have been no studies presenting local data on the surface of a single plate in a large array‡.

From the reviews cited earlier and this survey, it is clear that while the presence of vortex shedding in offset-strip arrays is well established, relatively few experimental studies show a direct link between increases in heat transfer and vortex shedding. Furthermore, the relative contributions of boundary layer restarting and vortex shedding for developing flows remains unclear. No studies have been found that analyze heat transfer in the developing region on a row-by-row basis over a range of Reynolds numbers, nor have any studies been found that present the local heat transfer behavior on a single fin in the offset-strip array. This research was undertaken to fill these gaps; to determine the relative impact of boundary-layer restarting and vortex shedding on heat transfer performance; to determine the nature of the flow field for developing conditions and the effect of this developing flow field on heat transfer; and to present unique data describing local heat transfer behavior along a fin. Using a simplified model that provides an essentially two-dimensional flow, this study will help develop a deeper understanding of the flow and its relation to the local, row-by-row, and average heat transfer behavior in offset-strip arrays.

† Zhang and Lang [10] report row-by-row results for a related louver (angled) geometry; however, they only used one naphthalene specimen in a large array.

‡ Suga and Aoki [12] reported numerically predicted local results for a related louver (angled) geometry at $Re = 192$ and $Re = 450$ (based on fin pitch). Their numerical predictions assumed steady flow and thus do not include vortex shedding effects.

EXPERIMENTAL METHOD

Mass transfer experiments were conducted to measure local and spatially averaged surface convective behavior, and complementary flow visualization experiments were used to obtain a clearer interpretation of the data. The mass transfer study used the naphthalene sublimation technique; thorough reviews of this method and its application have appeared previously [13–15]. The flow visualization experiments were conducted using ink injection in a conventional water tunnel. Descriptions of related experiments have been reported in the literature [3, 4, 9]. In this section, the apparatus, instrumentation, specimen preparation method, and experimental procedures will be presented. Data interpretation and uncertainty also will be discussed.

Apparatus and instrumentation

The induction wind tunnel shown schematically in Fig. 1 was used for the mass transfer experiments. During wind tunnel operation, air was drawn from the laboratory and discharged outside it to avoid contaminating the flow with naphthalene vapor. The laboratory relative humidity ($\pm 2\%$), temperature ($\pm 0.1°C$) and barometric pressure (± 13 Pa) were measured to infer the air density. The wind tunnel inlet was equipped with honeycomb flow straighteners, screens, and a 9-to-1 elliptic area contraction. A hot-wire anemometer was used to confirm that the approach velocity profile was flat to within approximately 2%, and the turbulence intensity was less than 2% (except as noted later) over the entire test range from 0.1 to 10 m s^{-1}. During normal mass transfer experimentation, the approach velocity in the 15.24×15.24 cm wind tunnel test section was inferred using a ASME Standard orifice plate located downstream of the test section (see Fig. 1(a)) and an electronic micromanometer (± 0.12 Pa).

The test section, shown schematically in Fig. 1(b), was constructed of acrylic and provided easy access to the instruments and test specimen array. Calibrated platinum RTDs were located 1.5 cm upstream and downstream of the test array to measure air temperature ($\pm 0.1°C$). Four static-pressure taps were located 2.5 cm upstream and downstream of the test array. The static pressure drop was measured using the electronic micromanometer or a calibrated capacitance-type pressure transducer (0–29 Pa, ± 0.37 Pa).

The test section accommodated up to 92 plates in eight rows as shown in Fig 2. For each experiment, from one to eleven naphthalene-coated specimens were placed in the middle columns of the test section (see Fig. 2). At low Reynolds numbers, eleven plates in a test array were naphthalene coated; eight were coated with naphthalene on one side, and three were

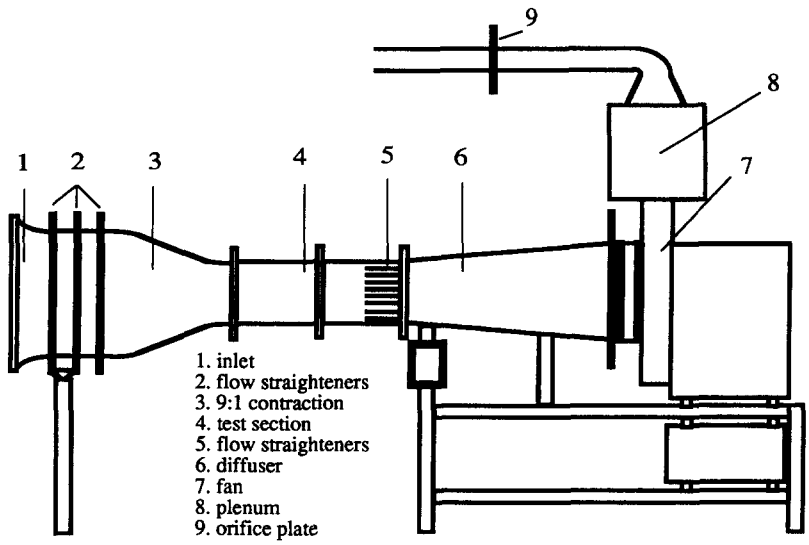

(a)

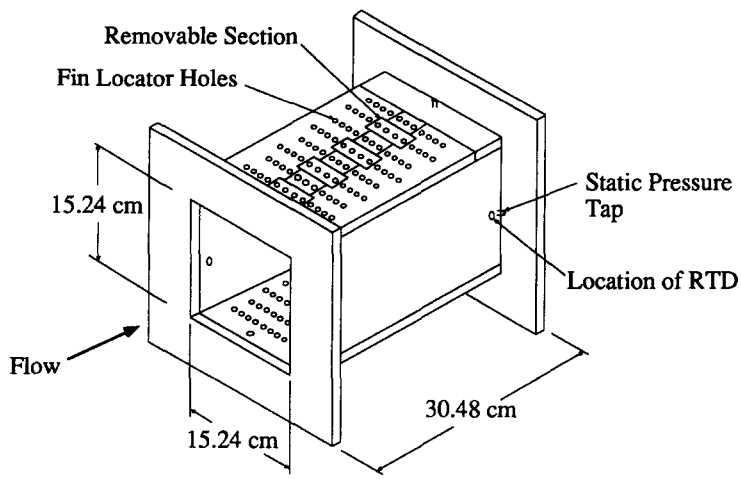

(b)

Fig. 1. (a) Schematic of the induction wind tunnel used for the mass transfer and pressure drop experiments; (b) schematic of the wind tunnel test section.

coated on both sides. The specimens were placed in the center of the test array to form a symmetric flow passage bounded by naphthalene-coated plates. For some high-Reynolds-number experiments, when the flow was well mixed, only two naphthalene-coated specimens were necessary. In these cases, the coated specimens were placed to face each other in the second-to-last row of the test array where the flow was fully developed. Uncoated plates were used for the rest of the array and provided proper flow conditions. All plates in the array were the same size and shape, and each plate completely spanned the 15.24 cm test section. Various arrangements were possible through minor changes in specimen mounting, and results will be reported for three arrangements. These arrays will be referred to as the *dense* geometry, the *sparse* geometry, and the *thin-plate* geometry (see Fig. 2)—these designations are only intended to remind the reader of the relative geometry of the array.

The naphthalene-coated specimens were constructed by pouring molten scintillation-grade naphthalene ($\sim 85°C$) onto the metal substrate of the test specimen ($\sim 25°C$). The naphthalene solidified in a shallow cavity on the specimen. After solidification, the excess naphthalene was mechanically removed, and the surface was polished with fine-grit sand paper.

A closed-loop water tunnel similar to the wind tunnel was used for flow visualization. Water was pumped through a plenum, honeycomb flow straighteners and a contraction before entering the test section. The test section was identical to that used in the wind tunnel

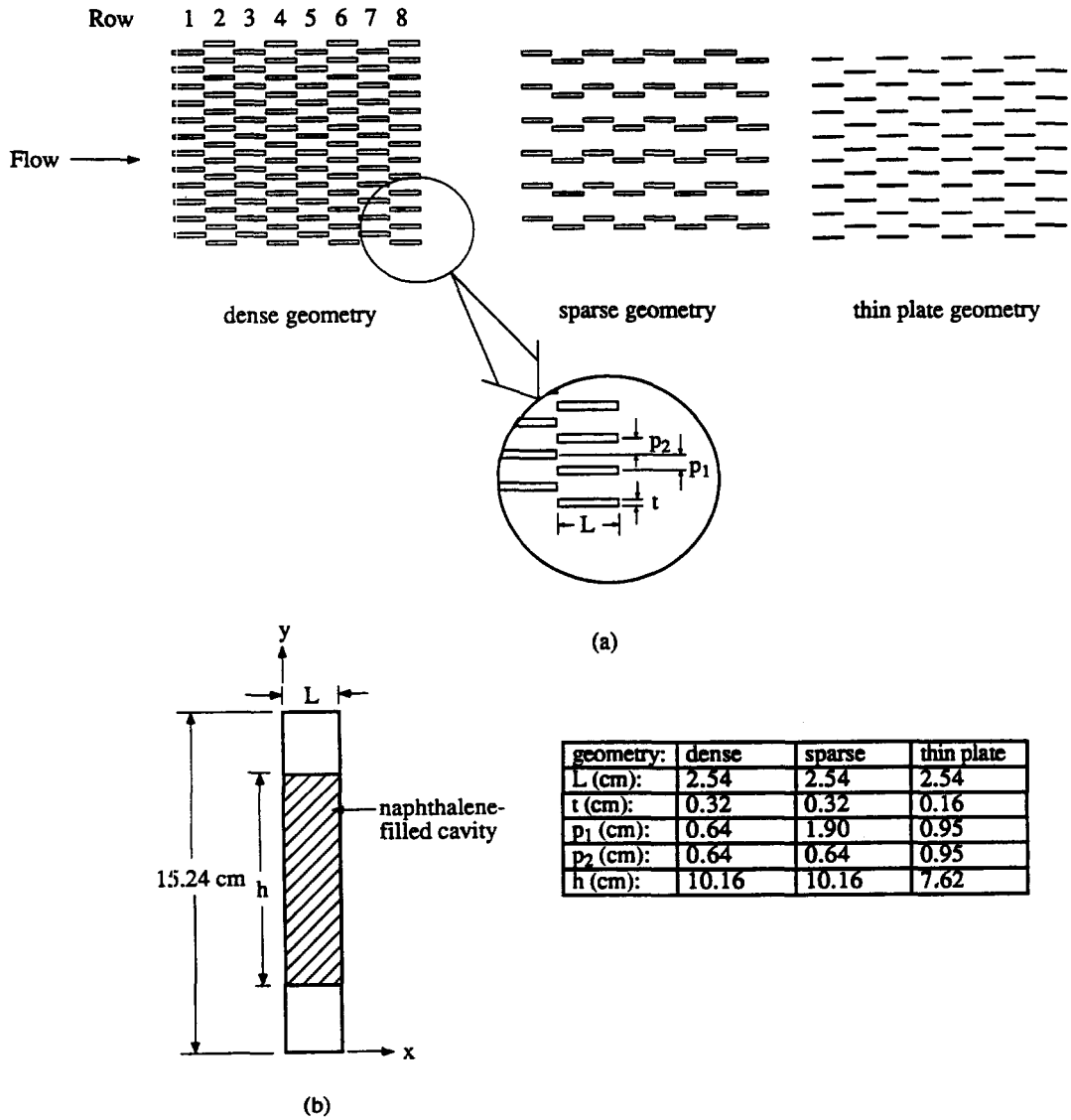

geometry:	dense	sparse	thin plate
L (cm):	2.54	2.54	2.54
t (cm):	0.32	0.32	0.16
p_1 (cm):	0.64	1.90	0.95
p_2 (cm):	0.64	0.64	0.95
h (cm):	10.16	10.16	7.62

Fig. 2. (a) Schematics of the three geometries: dense, $d_h = 16.9$ mm, sparse $d_h = 39.6$ mm, thin plate $d_h = 32.9$ mm; (b) schematic of a test specimen.

except that there was a short (8.9 cm) entrance section for dye injection. Dye was injected into the center of the channel about 2.5 cm upstream of the first fin. The dye was gravity fed through a 1.3 mm diameter needle with its end bent into the direction of the flow. The injection rate was regulated by a needle valve at the base of the dye reservoir. The test section was viewed through a mirror, and photographs were recorded using a 35 mm camera (see DeJong ref. [16] for details).

Experimental procedure

Before mass transfer experiments were conducted, the test specimens were weighed using an analytical balance (0–200 g, $\pm 5 \times 10^{-5}$ g). For cases where local data were obtained, the naphthalene surface profile was measured using a laser profilometer. This measurement system and its application to naphthalene sublimation have been described previously by Kearney and Jacobi [15, 17]. Those procedures were adopted in this work except that in the current study it was not necessary to add laser dye to the naphthalene. As in the earlier work, the laser profilometry system (Cyber-Scan 206) was subjected to a four-hour warm-up period to mitigate thermal drift. A 60-by-20-point scanning grid was used to cover a 7.62×2.54 cm test area centered on the naphthalene surface. Thus, each surface measurement point was taken to represent a surface area element of approximately 1.6 mm^2. On the basis of repeated scans of a reference surface, these optical methods provided sublimation depths with a 2-σ uncertainty of ± 6 μm. (This estimate is conservative in comparison to the manufacturer's specification of ± 4 μm; see also refs. [16] and [18].)

After weight and surface profile data were obtained,

the specimens were placed in the test array and exposed to a controlled air flow for a period ranging from 45 to 90 mins in duration, depending on the Reynolds number. At high Reynolds numbers, a short exposure period ensured that excessive sublimation did not cause significant geometrical distortion, whereas, at low Reynolds numbers, a longer exposure period was required to keep Sherwood number uncertainties acceptable (as discussed later). After exposure in the tunnel, the specimen was weighed and scanned again. A check for sublimation by natural convection during a scan was performed using a third (redundant) scan (see [19]); however, for the data reported in this paper, these corrections were always within the experimental uncertainty, so they were neglected. Likewise, the effect of natural sublimation during installation and removal of the specimens was checked by weighing a specimen, exposing it to the laboratory environment for a period equal to the installation and removal time (about three minutes), and re-weighing it. These tests proved that corrections for natural sublimation fell within the Sherwood number uncertainty. Therefore, this correction was also ignored for the mass averaged experiments.

During each run, upstream and downstream temperatures were sampled every 5 s and averaged over the period of the test. The upstream and downstream temperatures always differed by less than the uncertainty in the measurements. The core pressure drop, pressure drop across the orifice plate, relative humidity, barometric pressure, exposure time and fin mass were recorded during the experiment.

For flow visualization experiments in the water tunnel, ink was injected into the flow upstream of the first louver. The water velocity was determined by measuring the time necessary for a large ink marker in the flow to pass through the 20.3 cm long test section. Photographs were taken of flow behavior around individual louvers and throughout the array. At different flow velocities, the position of the first row of fins which shed vortices was recorded; however, as explained later, this observation required some judgment.

Data reduction and interpretation

The Reynolds number for flow through the test section was defined as

$$Re = \frac{U_c d_h}{\nu} \tag{1}$$

where U_c is the flow velocity at the minimum free-flow area, and d_h is the hydraulic diameter

$$d_h = \frac{2(p_1 + p_2 - t)L}{L + t}. \tag{2}$$

The definition of equation (2) neglects the wind tunnel walls, in essence assuming that the flow is two-dimensional. This approach was justified since the spanwise length was much larger than the other relevant length scales (t, p_1, p_2 and L); furthermore, the flow visualization results confirm that the important gross features of the flow are two-dimensional.

The average mass transfer coefficient was determined through

$$\bar{h}_m = \frac{\Delta m}{A_f \rho_{n,v} \Delta t} \tag{3}$$

where Δm is the change in mass of the specimen and Δt is the exposure time. The density of saturated naphthalene vapor was determined using the ideal gas law, and its vapor pressure was calculated using the correlation of Ambrose *et al.* [20].

Cho *et al.* [21] provided a correlation for the mass diffusivity and Schmidt number of naphthalene in air. The average Sherwood number was then calculated using

$$\overline{Sh} = \frac{d_h \bar{h}_m}{D_{na}}. \tag{4}$$

Following the suggestion of Sparrow and Hajiloo [2] for intermediate Schmidt numbers, a modified Colburn j factor was used for the spatially averaged mass transfer data

$$j = \frac{\overline{Sh}}{Re\, Sc^{0.4}}. \tag{5}$$

The core pressure drop, ΔP, was interpreted using the Fanning friction factor, f

$$f = \frac{2\Delta P}{\rho U_c^2}\left(\frac{d_h}{4L_{core}}\right). \tag{6}$$

The local mass transfer coefficients were determined from the sublimation depths using the following relation:

$$h_m = \frac{\rho_{n,s}\delta_{sb}}{\rho_{n,v}\Delta t} \tag{7}$$

where the density of solid naphthalene was taken to be 1162.0 kg m^{-3} per Kudchadker *et al.* [22]. Local Sherwood numbers could then be determined from

$$Sh = \frac{h_m d_h}{D_{na}}. \tag{8}$$

As a redundant check, the local Sherwood numbers were integrated and compared to the mass-averaged Sherwood numbers using the following approximation:

$$\overline{Sh}_{int} = \frac{1}{A}\int_A Sh\, dA \approx \frac{1}{N}\sum Sh. \tag{9}$$

If $\overline{Sh}_{int}$ from equation (9) were not within 10% of $\overline{Sh}$ as determined from the weight data (equation 4), the local data were rejected.

Uncertainty

The uncertainties of the reduced data were determined by propagating the measurement uncertainties using standard methods [23]. The uncertainty in Re was 2% for the mass transfer experiments and less then 10% for the flow visualization experiments. The uncertainty in Sh was less then 5% while the uncertainty in the modified Colburn j factor was 5.5%. The uncertainty in sublimation depth depended on the magnitude of the sublimation depth. During a typical run, sublimation depths ranged from 25 μm up to about 120 μm with an average of approximately 60 μm. These values yielded an average uncertainty in local Sherwood number of 11% with an uncertainty of 24% in regions of low mass transfer and 7% in regions of high mass transfer. The average sublimation depth represented less than a 2% change in plate thickness for the thick plates and about 3% for the thin specimens. The uncertainty in ΔP decreased as the Reynolds number increased because the uncertainty of the pressure measurement was fixed. Therefore, the uncertainties in ΔP ranged from approximately 50% at very low Reynolds numbers to 0.2% at high Reynolds numbers. Above a Reynolds number of 1000, the average uncertainty in ΔP was 1%, leading to an average uncertainty in f of about 4%.

RESULTS

Flow visualization

Flow visualization results for the dense geometry are given in Fig. 3 for Reynolds numbers ranging from 380 to 1060. The photographs shown in the figure depict select portions of the 92-plate array—only the center columns are shown, and the row numbers are labeled. Because the visual results can depend on where ink was injected, multiple photographs are shown at one Reynolds number. While a retaining tab can be seen in some photographs (in the middle third of a plate), this tab was buried in the water tunnel wall, and the test section was completely spanned by the test specimen.

At $Re = 380$, the flow was steady and laminar through the entire array as shown in Fig. 3(a). At this Reynolds number, steady recirculating eddies formed in the wake of each plate. This behavior was observed at higher Reynolds numbers ($Re = 460$); however, by $Re = 550$, a distinct change in flow structure was evident as shown in Fig. 3(b). A periodic secondary flow structure formed at the fourth or fifth row. This secondary structure was small relative to the plate and difficult to see at this Reynolds number. For these conditions, the array wake exhibited a 'feathery appearance' that we have not found reported in the literature. On the basis of these observations, we speculate that the periodic secondary structures were small-scale transverse vortices shed at the fourth row. Apparently, these vortices were stretched by a velocity gradient in the main flow (i.e. $\partial u/\partial z$). The feathery wake of Fig. 3(b) then consists of secondary vortices stretched by a velocity gradient and advected downstream.

At higher Reynolds numbers, the wake took the roughly sinusoidal appearance reported by others. This behavior is shown for $Re = 630$ in Fig. 3(c), where secondary structures appear at the fourth row. These structures were still of a small scale relative to the plates, and they were sometimes difficult to identify. However, by a Reynolds number of 720, large-scale vortex shedding was obvious in the array. This flow is shown in Fig. 3(d). The wake now closely resembled the classical Kármán vortex street. At this Reynolds number, it was clear from the flow visualization results that vortex shedding occurred at the leading edges of the plates. The scale of the vortices was much larger at $Re = 720$ than at $Re = 630$. For these conditions, the secondary structures did not appear distorted at the back of the array, suggesting that the velocity distribution was different under these conditions. It seems reasonable to speculate that as the Reynolds number increased, the magnitude of the transverse velocity fluctuations associated with the secondary structures increased. These fluctuations appeared to be related to shedding at the leading edge and to result in less distortion of the vortices as they were advected downstream.

For higher Reynolds numbers still, the onset of vortex shedding occurred earlier in the array. For $Re = 850$, as shown in Fig. 3(e), vortex shedding was apparent at the third row in the array, and a discrete flow structure was maintained throughout the eight-row array. The wake clearly exhibited a vortex street, and vortices emerged from the array without obvious stretching (cf. Fig 3(b)). At higher Reynolds numbers the entire array shed vortices, and for yet higher Reynolds numbers a transition to turbulence occurred. In Fig. 3(f), it appears that for $Re = 1060$ the first row was shedding vortices, and the flow was turbulent by about the sixth row.

For developing flow through an array of flat plates, the flow is laminar and steady (as expected) at low Reynolds numbers. With an increase in the Reynolds number, plates downstream in the array begin to shed vortices. Initially, shedding occurs in a flow with a relatively high velocity gradient normal to the plate surface; this gradient significantly stretches and distorts the vortices as they are carried to the array exit. In accordance with the deep-array observations by Mochizuki and Yagi [3] and in contrast to the shallow arrays results of Mullisen and Loehrke [5], the onset of vortex shedding moves upstream in the array as the Reynolds number is increased. Although it is not clearly established by our flow visualization results, we speculate on the basis of these earlier studies that shedding first occurs at the trailing edge of the last row. Once shedding moves forward to the trailing edge of the second-to-the-last row, the leading edge of the last row sheds. This behavior occurs earlier in the array at higher Reynolds numbers.

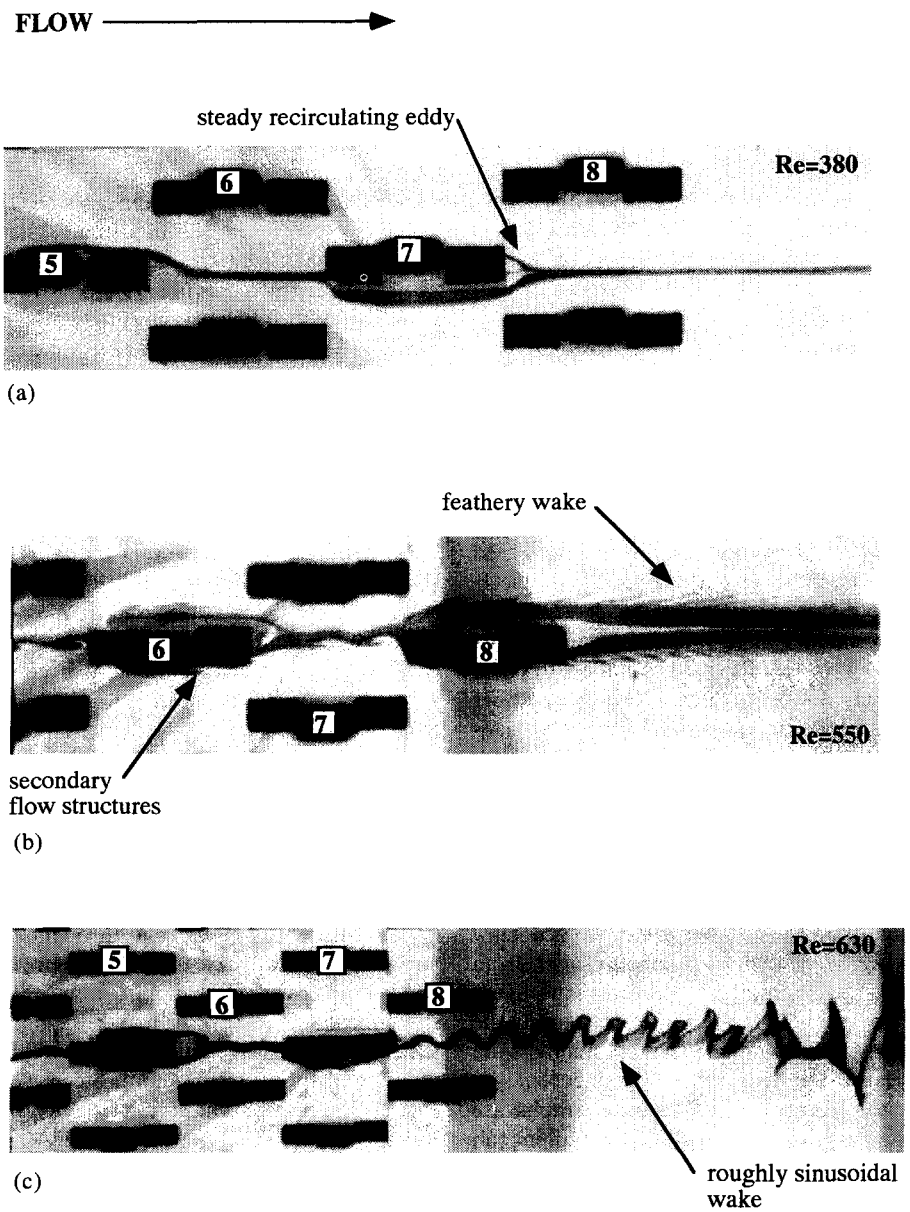

Fig. 3. Water tunnel flow visualization results for the dense geometry: (a) $Re = 380$, rows 5–8; (b) $Re = 550$, rows 6–8; (c) $Re = 630$, rows 5–8; (d) $Re = 720$, rows 4–8; (e) $Re = 850$, rows 2–8; (f) $Re = 1060$, rows 2–8. (*Continued opposite.*)

While we never observed shedding from the leading edge of the first row, shedding from the leading edge of the second and subsequent rows in the array was clearly identified. When an upstream plate produces transverse velocity fluctuations, flow at the downstream plate may separate at alternate corners of its leading edge—this coupling causes vortex shedding at the leading edge of the plate. The first row cannot be subjected to such oscillations. (There are no upstream plates to cause the fluctuations.) This explanation will be discussed further when row-by-row mass transfer results are presented. Vortices are shed from the leading edges of the plates and appear to increase in size (to some maximum) as the Reynolds number increases. In the vortex shedding regime, the flow is periodic, and the vortices have a constant spacing and structure. The Strouhal number (based on fin thickness) was estimated from the flow visualization to be constant at approximately 0.32 over the range of Reynolds numbers in which vortex shedding was observed (see DeJong [16] for a more detailed account). This value agrees with the work of Xi *et al.* [9] for a similar geometry to within the experimental uncertainty. Once the entire array is shedding, a further increase in the Reynolds number can cause the flow to become turbulent. It is unclear from the flow visualization results whether vortex shedding occurs in the turbulent flow regime.

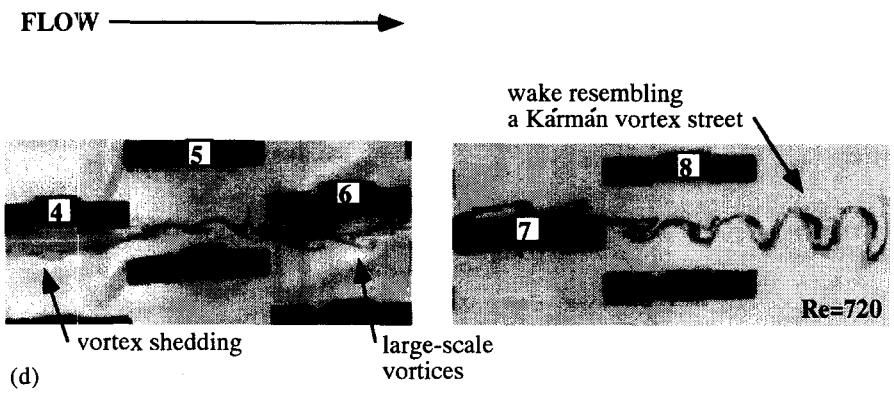

(d)

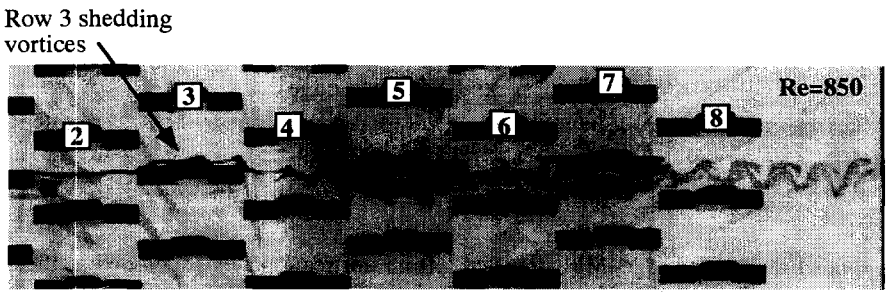

(e)

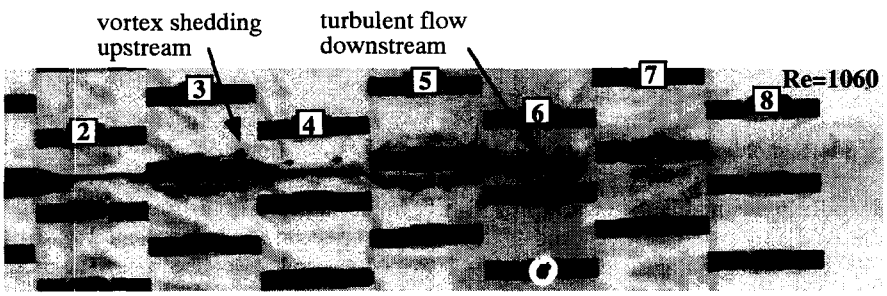

(f)

Fig. 3—*continued.*

Local and row-by-row mass transfer data

Results from local mass transfer experiments for several Reynolds numbers in the dense geometry are given in Fig. 4. For each case, these results were obtained for a plate in the seventh row of the array. The coordinate, x^*, is measured from the leading edge to the trailing edge of one specimen (see Fig. 2). For each point on the plot (at a fixed position in x^*) 60 sublimation depths were measured by surface profilometry in the spanwise (y) direction and averaged. Thus, each point in the plot represents an average of 60 surface measurements. This procedure was adopted because no spanwise variation in the local Sherwood number was observed for these experiments—a result reflecting the two-dimensionality of the flow.

At a relatively low Reynolds number, $Re = 380$, the local mass transfer behavior shown in Fig. 4 reflects the development of a boundary-layer; transport is high near the leading edge and decreases in the downstream direction. At this position in the array, boundary-layer restarting occurs in a flow with a fully developed, periodic velocity profile. While the details of the local distribution may change at other positions in the array (e.g. for a developing velocity profile), the overall trends will reflect boundary layer restarting for every plate in the array.

At higher Reynolds numbers, vortex shedding has a profound effect on the local mass transfer behavior. The $Re = 773$ case shown in Fig. 4 corresponds to the vortex shedding regimes shown in Fig. 3. The time-averaged local mass transfer near the leading edge is low; it increases in the downstream direction, reaches a maximum near a position of $x^* = 0.2$ and decreases as the flow approaches the trailing edge. This behavior suggests that in a time-averaged sense, vortex formation at the leading edge results in a separation and

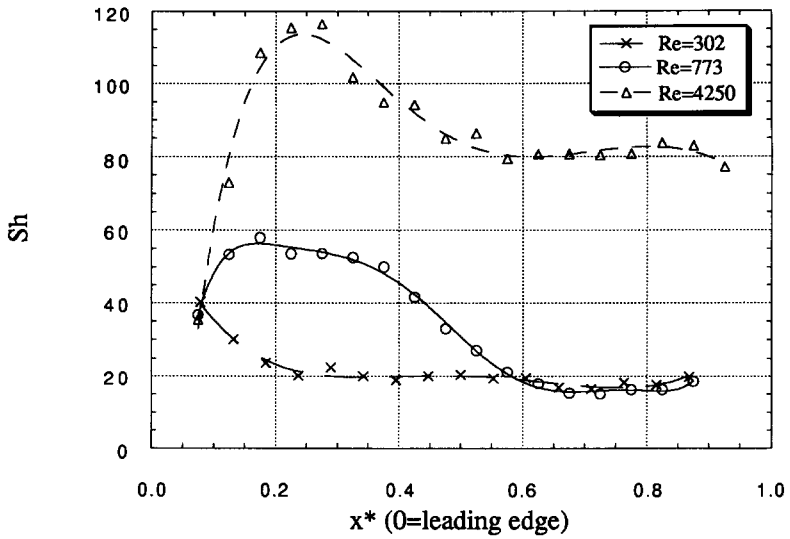

Fig. 4. Local Sherwood number distributions in row 7 of the dense geometry at three different Reynolds numbers.

recirculation zone at the leading edge. Mass transfer dramatically increases due to the inward normal flow associated with the vortex forming at the leading edge. This time-averaged view is only loosely descriptive, but certainly the normal (transverse) velocity plays a role in the convective mass (heat) transfer. After vortices are shed, they are advected downstream and increase the local heat transfer due to mixing. While the details of this distribution will vary with position in the array and Reynolds number, the trends are expected to occur whenever shedding is present.

At the highest Reynolds number shown in Fig. 4, $Re = 4250$, the flow appears to be turbulent at the seventh row. It is very interesting to note the similarities in local behavior under these conditions and the $Re = 773$ case. In both cases, the local Sherwood number increases to a maximum near $x^* = 0.2$ and then decreases. This similarity may be because the plate is shedding vortices; unfortunately, we are unable to determine from flow visualization whether shedding occurred in the turbulent regime. An alternative explanation is that steady leading-edge separation occurred at $Re = 4250$, and the boundary-layer re-attached at about $x^* = 0.2$. Mass transfer is high in the attachment region and decreases as the turbulent boundary layer grows. We expect that the local trends shown for $Re = 4250$ will extend to other locations and Reynolds numbers where the flow is locally turbulent in the array.

In Fig. 5(a), Sherwood numbers for specimens in successive rows of the dense geometry are plotted at various Reynolds numbers. At low Reynolds numbers, where the flow is laminar and no shedding occurs, the Sherwood numbers decrease slightly for successive downstream rows in the array. This decrease is a development effect at low Reynolds numbers. Since the flow is not well mixed, boundary-layers from upstream plates are carried to the downstream plates, decreasing their Sherwood numbers. As the Reynolds number increases, vortex shedding begins in the downstream rows and moves forward in the array. Because shedding increases the convective transport, once a plate begins to shed from its leading edge, its Sherwood number will increase. From both the row-by-row mass transfer data (Fig. 5(a)) and the flow visualization results (Fig. 3), it appears that for $Re \approx 550$, shedding occurred in row 5; for slightly higher Reynolds numbers up to $Re \approx 775$, shedding began in row 4. For Reynolds numbers from about 800–900, shedding was present by row 3; and for $Re > 1000$, row 2 was shedding. The presence of vortex shedding in only the last rows of the array was not observed; however, Mochizuki and Yagi [3] found that at low Reynolds numbers, a small change in Reynolds number caused a large change in the location of vortex shedding. Thus, it is likely that our specific Reynolds numbers did not allow for the onset of shedding late in the array.

It is interesting to note that for very high Reynolds numbers ($Re > 1000$), an increase in Sherwood number from row 1 to row 2 was always observed while vortex shedding from the leading edge of row 1 was never observed in the flow visualization experiments. This result suggests that row 1 did not shed at its leading edge, but that perhaps it shed from its trailing edge, and due to the associated transverse velocity fluctuations, row 2 subsequently shed from its leading edge. Thus, the velocity oscillations caused by the first row caused the second row to shed at the leading edge. This behavior was also observed for the sparse geometry.

From Fig. 5(b) it is clear that flow through the sparse geometry has a higher critical Reynolds number than flow through the dense geometry. The mass

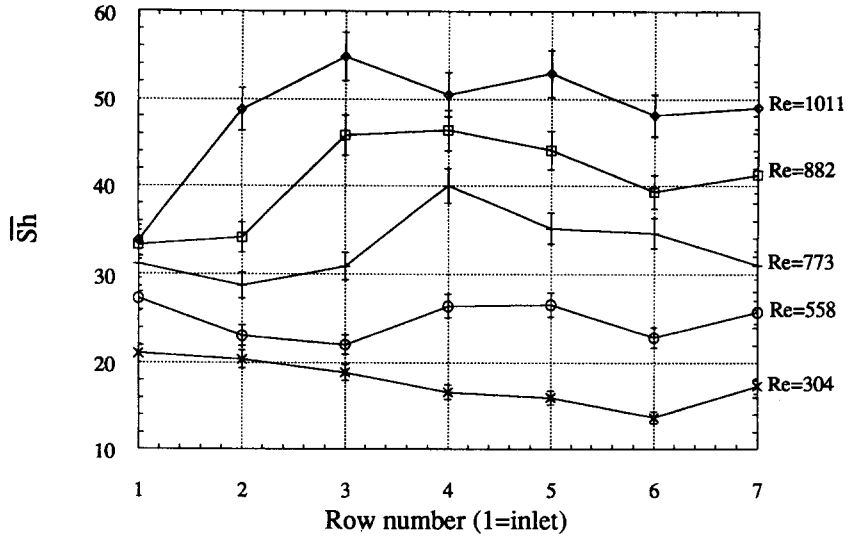

(a)

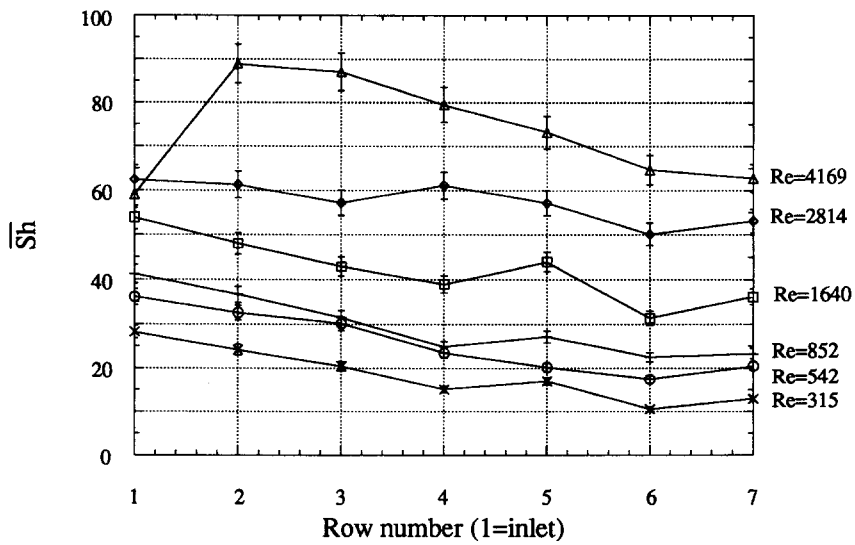

(b)

Fig. 5. Row-by-row Sherwood numbers for (a) the dense geometry and (b) the sparse geometry.

transfer results suggest that there is no shedding at $Re = 852$. Perhaps there is no shedding (or very small-scale structures are shed) for Reynolds numbers as high as $Re = 2814$. Certainly, by $Re = 4169$ the entire array is shedding, and a large increase in Sh is evident at row 2. The mass transfer results alone do not allow a clear distinction between the vortex shedding and turbulence effects. However, that vortex shedding occurs at a higher Reynolds number in the sparse geometry is clearly supported. Even if the same length scale is used for both geometries (e.g. the plate thickness, t), the critical Reynolds number is higher for the sparse geometry. This result is in agreement with Xi and co-workers [9], who found that the flow became more unstable as the fin pitch decreased.

Developed-flow data

Experimental Colburn j and Fanning friction factors for the three geometries are presented in Fig. 6. The mass transfer data were acquired from specimens in the sixth and seventh rows of the array. The mass transfer data for the dense geometry show more scatter than the others. (It was found that the approach turbulence intensity was higher, nearer 3% rather than below 2%, for some of these data.) The correlations of Wieting [24] and Joshi and Webb [6] have been reformulated to use the definition of hydraulic diameter adopted in this work. These correlations should be compared only to the thin-plate geometry since the geometrical parameters for that case were closest to those used in their development. Both the exper-

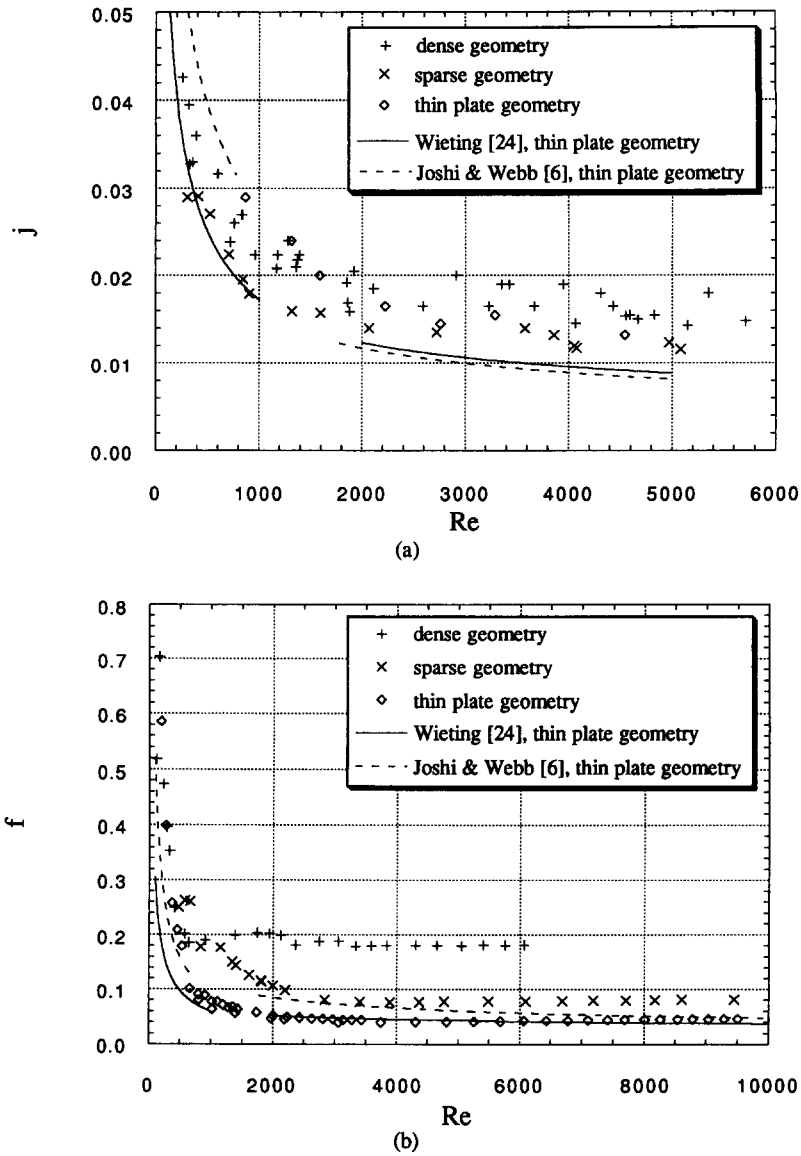

Fig. 6. (a) Modified Colburn j factors for specimens in rows 6 and 7. (b) Friction factors for the three geometries. Correlations from the literature for both j and f use parameters for the thin plate geometry.

imental j and f factors show relatively good agreement with the correlations. The disagreement in j factor may be because a constant-temperature boundary condition was simulated in the current mass transfer experiments, but the heat transfer data were obtained under different conditions. (In some cases the boundary conditions are not clearly reported.)

At low Reynolds numbers, the j factors for the three geometries are similar. Kurosaki *et al.* [11] found that streamwise spacing has a much larger effect on heat transfer than does fin pitch, and an identical streamwise spacing was used for these geometries. At higher Reynolds numbers, above approximately $Re = 800$, the dense geometry performs somewhat better than the others, perhaps because the flow through the dense array makes the transition to periodic flow earlier than flow through the other two arrays with larger fin pitches. The small fin pitch in the dense geometry would also cause vortex shedding to have a larger effect on neighboring plates.

The relative contributions of boundary layer restarting and vortex shedding can be identified using the results presented in Fig. 7. The correlations of Shah and London [25] are for the thermal entry length between parallel plates of constant and equal temperatures. Their correlations were developed as a simplified approximation to full solution of the momentum and energy equations. In the figure, two 'theoretical' calculations are presented: (i) a continuous plate solution (17.78 cm long plates) and (ii) an interrupted plate solution (2.54 cm long interrupted parallel plates). The difference between these

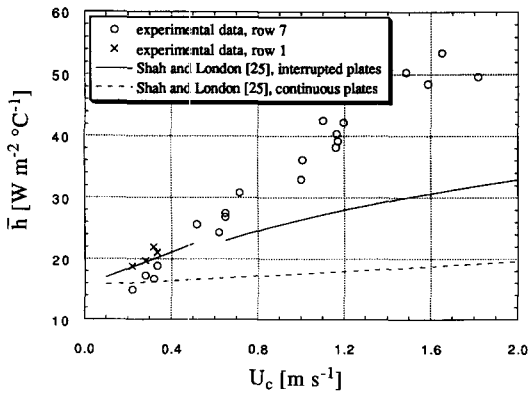

Fig. 7. Experimental and theoretical average heat transfer coefficients; all experimental data taken in row 7 of the dense geometry.

two correlations thus represents the effect of boundary-layer restarting†. At low Reynolds numbers, the mass transfer data from row 1 are in good agreement with the interrupted fin result, and the data from row 7 are in good agreement with the continuous fin result. This behavior indicates that at low Reynolds numbers, mixing between the rows is insufficient to provide the full boundary-layer restarting effect. The boundary-layers from upstream plates flow (partially intact) onto downstream plates and decrease their performance. At higher Reynolds numbers, the experimental values are significantly larger than the theoretical values for an interrupted surface because of vortex shedding. The figure demonstrates that the relative contributions of boundary-layer restarting and vortex shedding depend on the Reynolds number. At low Reynolds numbers ($Re < 430$; $U_c < 0.4$ m s^{-1}) there is no vortex shedding, and boundary-layer restarting effects are diminished due to insufficient mixing. For a Reynolds number where the array is expected to be in the laminar vortex shedding regime ($Re = 850$; $U_c = 0.8$ m s^{-1}), boundary-layer restarting accounts for approximately a 40% increase over the continuous fin result, and vortex shedding accounts for roughly another 40% increase. In other words, in this regime vortex shedding and boundary-layer restarting are both important mechanisms for heat transfer. For $Re > 1200$ ($U_c > 1.1$ m s^{-1}) turbulence effects are expected to be important through a large portion of the array, and only limited results at these higher Reynolds numbers have been presented in Fig. 7.

SUMMARY AND CONCLUSIONS

An experimental study of flow and heat transfer in arrays of parallel, flat plates was presented with the objective of developing a deeper understanding of the heat transfer mechanisms in this geometry. Complementary flow visualization and local, row-by-row, and spatially averaged mass transfer experiments were conducted for the dense geometry; row-by-row and spatially averaged mass transfer data were presented for the sparse geometry; and only fully developed, spatially averaged results were presented for the thin-fin geometry. Friction factor data were also presented for each array. The averaged mass transfer behavior and friction factor data were found to be in reasonable agreement with previously published results for similar geometries.

A direct link between vortex shedding and heat transfer behavior was established for these geometries. For steady laminar flow, the local Sherwood number distribution on a specimen surface was highest at the leading edge and decreased as the boundary layer developed. For higher Reynolds numbers, when vortex shedding occurred, the local Sherwood number increased to a maximum near a location of $x^* = 0.2$ on the plate and then decreased as the flow approached the trailing edge. This distribution was related to the formation and shedding of vortices and the boundary-layer behavior—both mechanisms are important. For turbulent conditions, a similar Sherwood number distribution was observed; however, it was not possible to determine whether these similarities were due to vortex shedding in the turbulent regime.

Using the flow visualization results and the row-by-row mass transfer data, it was possible to identify the position within the dense geometry where the onset of shedding occurred. Shedding began first in the downstream rows and occurred farther upstream as the Reynolds number increased. Apparently, the first row of the array did not shed from its leading edge, but the second and subsequent rows did shed from their leading edges. Shedding began at lower Reynolds numbers for the dense geometry.

Using the row-by-row and fully developed results and comparing these data to theoretical solutions for developing channel flows, the relative contributions of boundary layer restarting and vortex shedding to heat transfer for an offset-strip array were determined. At low Reynolds numbers, where no vortex shedding occurred, mass transfer results downstream in the array fell below the theoretical interrupted plate solution because the flow was not well mixed. At higher Reynolds numbers, vortex shedding caused the mass transfer results to be significantly above the interrupted-plate solution.

Acknowledgements—This research was supported by the Air-Conditioning and Refrigeration Center (ACRC) at the University of Illinois. The ACRC is a National Science Foundation, industry and university cooperative research center. The first author is partially supported through an ASHRAE Grant-in-aid. Both authors are indebted to Dr L. Zhang and Prof. S. Balachandar for discussions and insights gained through their related work.

† Two curves are shown for the interrupted surface because two correlations were needed to span the experimental range.

REFERENCES

1. Manglik, R. M. and Bergles A. E., Heat transfer and pressure drop correlations for the rectangular offset strip fin compact heat exchanger. *Experimental Thermal Fluid Science*, 1995 **10,** 171–180.
2. Sparrow, E. M. and Hajiloo, A., Measurements of heat transfer and pressure drop for an array of staggered plates aligned parallel to an air flow. *Journal of Heat Transfer*, 1980, **102,** 426–432.
3. Mochizuki, S. and Yagi, Y., Characteristics of vortex shedding in plate arrays. In *Flow Visualization II*, ed. W. Merzkirch. Washington, DC, Hemisphere, pp. 99–103.
4. Mochizuki, S., Yagi, Y. and Yang, W., Transport phenomena in stacks of interrupted parallel-plate surfaces. *Experimental Heat Transfer*, 1987, **1,** 127–140.
5. Mullisen, R. S. and Loehrke, R. I., A study of the flow mechanisms responsible for heat transfer enhancement in interrupted-plate heat exchangers. *Journal of Heat Transfer*, 1986, **385,** 377–385.
6. Joshi, H. M. and Webb, R. L., Heat transfer and friction in the offset strip-fin heat exchanger. *International Journal of Heat and Mass Transfer*, 1987, **30,** 69–83.
7. Amon, C. H. and Mikic, B. B., Spectral element simulations of forced convective heat transfer: application to supercritical slotted channel flows. In *National Heat Transfer Conference: Numerical Heat Transfer With Personal Computers and Supercomputing*, HTD-Vol. 110. ASME, New York, 1989, pp. 175–183.
8. Amon, C. H., Majumdar, D., Herman, C. V., Mayinger, F., Mikic, B. B. and Sekulic, D. P., Experimental and numerical investigation of oscillatory flow and thermal phenomena in communicating channels. In *Experimental/Numerical Heat Transfer in Combustion and Phase Change*, HTD-Vol. 170, ASME, New York, 1991, pp. 25–34.
9. Xi, G., Futagami, S., Hagiwara, Y. and Suzuki, K., Flow and heat transfer characteristics of offset-fin array in the middle Reynolds number range. In *ASME/JSME Thermal Engineering Proceedings*, Vol. 3. ASME, New York, 1991, pp. 151–156.
10. Zhang, H. and Lang, X., The experimental investigation of oblique angles and interrupted plate lengths for louvered fins in compact heat exchangers. *Experimental Thermal Fluid Science*, 1989, **2,** 100–106.
11. Kurosaki, Y., Kashiwagi, T., Kobayashi, H., Uzuhashi, L. and Tang, S., Experimental study on heat transfer from parallel louvered fins by laser holographic interferometry. *Experimental Thermal Fluid Science*, 1988, **1,** 59–67.
12. Suga, K. and Aoki, H., Numerical study on heat transfer and pressure drop on multilouvered fins. In *ASME/JSME Thermal Engineering Proceedings*, Vol. 4. ASME, New York, 1991, pp. 361–368.
13. Goldstein, R. J. and Cho, H. H., A review of mass transfer measurements using naphthalene sublimation, *Experimental Thermal Fluid Science*, 1995, **10,** 416–434.
14. Souza Mendes, P. R., The naphthalene sublimation technique. *Experimental Thermal Fluid Science*, 1991, **4,** 510–523.
15. Kearney, S. P. and Jacobi, A. M., Local convective behavior and fin efficiency in shallow banks of inline and staggered, annularly finned tubes. *Journal of Heat Transfer* 1996, **118,** 317–326.
16. DeJong, N. C., An experimental study of flow and heat transfer in offset strip and louvered-fin heat exchangers. M.Sc thesis, University of Illinois at Urbana-Champaign, Urbana, IL, 1995.
17. Kearney, S. P. and Jacobi, A. M., Effects of gull-wing baffles on the performance of a single-row, annularly finned tube heat exchanger. *International Journal of HVAC & R Research*, 1995, **1,** 257–272.
18. Kearney, S. P., Local and average heat transfer and pressure drop characteristics of annularly finned tube heat exchangers. M.Sc thesis, University of Illinois at Urbana-Champaign, Urbana, IL, 1995.
19. Hu, X. and Jacobi, A. M., Local heat transfer behavior and its impact on a single row, annularly finned tube heat exchanger. *Journal of Heat Transfer*, 1993, **115,** 66–74.
20. Ambrose, D., Lawrenson, I. F. and Sprake, C. H. S., The vapor pressure of naphthalene. *Journal of Chemical Thermodynamics*, 1975, **7,** 1173–1175.
21. Cho, K., Irvine, T. F. and Karni, J., Measurement of the diffusion coefficient of naphthalene into air. *International Journal of Heat and Mass Transfer*, 1992, **35,** 957–966.
22. Kudchadker, A. P., Kudchadker, S. A. and Wilhoit, R. C., *Naphthalene*. American Petroleum Institute, Washington, DC, 1978.
23. Kline, S. J. and McClintock, F. A., Describing uncertainties in single sample experiments. *Mechanical Engineering*, 1953, **75,** 3–8.
24. Wieting, A. R., Empirical correlations for heat transfer and flow friction characteristics of rectangular offset-fin plate-fin heat exchangers. *Journal of Heat Transfer*, 1975, **97,** 488–490.
25. Kays, W. M. and Perkins, H. C., Forced convection, internal flow in ducts. In *Handbook of Heat Transfer Fundamentals*, 2nd edn, Chap. 7, ed. W. M. Rohsenow, J. P. Hartnett and E. N. Ganiç. McGraw-Hill, New York, 1985.